Generation of Mesoscale Gravity Waves in Upper-Tropospheric Jet–Front Systems

FUQING ZHANG

Department of Atmospheric Sciences, Texas A&M University, College Station, Texas

(Manuscript received 8 April 2003, in final form 19 August 2003)

ABSTRACT

Multiply nested mesoscale numerical simulations with horizontal resolution up to 3.3 km are performed to study the generation of mesoscale gravity waves during the life cycle of idealized baroclinic jet–front systems. Long-lived vertically propagating mesoscale gravity waves with horizontal wavelengths ~100–200 km are simulated originating from the exit region of the upper-tropospheric jet streak, in a manner consistent with past observational studies. The residual of the nonlinear balance equation is found to be a useful index in diagnosing flow imbalance and predicting wave generation. The imbalance diagnosis and model simulations suggest that balance adjustment, as a generalization of geostrophic adjustment, is likely responsible for generating these mesoscale gravity waves. It is hypothesized that, through balance adjustment, the continuous generation of flow imbalance from the developing baroclinic wave will lead to the continuous radiation of gravity waves.

1. Introduction

Gravity waves are ubiquitous in the atmosphere and play a fundamental role in a wide variety of atmospheric processes. They can transfer significant amounts of energy and momentum (e.g., Eliassen and Palm 1960), initiate and organize convection (Zhang et al. 2001 and references therein), and generate and modulate atmospheric turbulence (e.g., Shapiro 1981). The momentum transport and deposition by gravity waves have significant impacts on the general circulation of the atmosphere (e.g., Holton et al. 1995). A better knowledge of these processes demands a complete understanding of the mechanisms by which the gravity waves are generated, together with their characteristics, distribution, and variability (Fritts 1984).

Mesoscale gravity waves with amplitude of 1–15 hPa, wavelength of 50–500 km, and periods of 0.5–4 h have been shown to be very important to sensible weather. Such mesoscale gravity waves can be generated by convection, density impulses and cross-frontal ageostrophic accelerations, shear instability, topographic forcing, and geostrophic adjustment related to jets, fronts, and/or sources of strong diabatic heating (Hooke 1986). From the examination of 13 observed tropospheric gravity wave events, Uccellini and Koch (1987, hereafter referred to as UK87) found that mesoscale gravity waves frequently appear in the vicinity of jet streaks and to the cold air side of a surface frontal boundary. They suggested that such waves are generated as an upper-level jet streak propagates away from a geostrophic wind maximum at the base of the geopotential height trough toward an inflection point in the height field. They conjectured that such a flow is unbalanced and thus would be adjusted in the sense that air parcels would accelerate in the exit region when quasi- and semigeostrophic theory dictates that the opposite kind of behavior is needed to maintain thermal wind balance.

From idealized simulations of baroclinic wave life cycles with a 3D hemispheric primitive equation model, O'Sullivan and Dunkerton (1995, hereafter referred to as OD95) demonstrated that gravity waves arose spontaneously as the tropospheric jet stream was distorted by baroclinic instability and strong parcel accelerations took place, primarily in the exit region of the upper-tropospheric jet streaks. However, because of the limited horizontal resolution (~100 km) they used, only subsynoptic scale inertia–gravity waves with horizontal wavelengths of 600–1000 km were generated in the simulations. Even though the scales and other characteristics of the inertia-gravity waves did not change substantially when they doubled the model resolution, the hemispheric model with ~50 km resolution was still too coarse to resolve and demonstrate the emission of *mesoscale* gravity waves from baroclinic instability.

Nevertheless, it is *mesoscale* gravity waves with horizontal wavelength of 50–500 km that are found to be prevalent in the vicinity of the unbalanced upper-level jet streaks. This has been demonstrated repeatedly from observational studies of gravity waves (e.g., UK87; Schneider 1990; Fritts and Nastrom 1992; Ramamurthy et al. 1993; Bosart et al. 1998; Thomas et al. 1999;

Corresponding author address: Dr. Fuqing Zhang, Dept. of Atmospheric Sciences, Texas A&M University, College Station, TX 77845-3150.
E-mail: fzhang@tamu.edu

© 2004 American Meteorological Society

Koppel et al. 2000; Rauber et al. 2001) and numerical investigations of the observed cases (e.g., Powers and Reed 1993; Zhang and Koch 2000; Zhang et al. 2001; Koch et al. 2001). These mesoscale waves may have a greater impact on the transport of momentum than the subsynoptic waves (Fritts and Nastrom 1992). It is also *mesoscale* gravity waves that are intimately linked to the initiation and modulation of convection (e.g., Raymond 1976; Lindzen 1974; Powers 1997; Lane and Reeder 2001; Zhang et al. 2001).

The aim of this paper, complementary to the work of OD95, is to explore the initiation and characteristics of *mesoscale* gravity waves through baroclinic instability using extremely high-resolution simulations of the life cycle of baroclinic waves from a multiply nested mesoscale model. A brief introduction to the numerical model, initial conditions, and experimental design for the work will be presented in section 2, followed in section 3 by a description of the evolution and structure of an idealized baroclinic wave simulation. Section 4 will present an analysis of the characteristics of the gravity waves simulated in the control experiment described in section 3. The impacts of model resolution and diffusion are explored in section 5. Diagnosis of the flow imbalance and discussions on the wave generation dynamics are presented in section 6. Section 7 contains a summary.

2. Experimental design

a. Model and experiments

To study the initiation of mesoscale gravity waves within an evolving baroclinic jet-front system, the control simulation (CNTL) with the fifth generation Pennsylvania State University–National Center for Atmospheric Research (NCAR–PSU) Mesoscale Model (MM5, version 2: Dudhia 1993) employs three model domains (D1, D2, D3) with 90-, 30-, and 10-km horizontal grid spacing, respectively, and 60 vertical layers with 360-m vertical spacing. The model vertical layers are chosen so that grid levels are approximately equally spaced in height. For simplicity the model is run in Cartesian coordinates with the Coriolis parameter constant. Here D1 is configured in the shape of a channel 27 000 km long (x direction) and 8010 km wide (y direction) with fixed lateral boundary conditions, and D2 (D3) is a rectangular subdomain 9300 (3100) km long and 4500 (2500) km wide centered at $x = 6150$ (17 000) km and $y = 2850$ (6700) km within D1 (D2). Two-way nesting is used for the lateral boundary conditions for D2 and D3. Radiative top boundary conditions are employed for all these model domains. Moist processes, surface fluxes, and friction are all neglected in the simulations.

For the control experiment, the coarse domain (D1) is integrated 120 h using balanced initial conditions (detailed below). Domain D2 (D3) is initialized at 60 (84) h from the solution on D1 (D2) and integrated for 60 (36) h with boundary conditions provided to D2 (D3) by D1 (D2) through two-way nesting. Experiments testing sensitivity to model resolution and diffusion will be described in section 5.

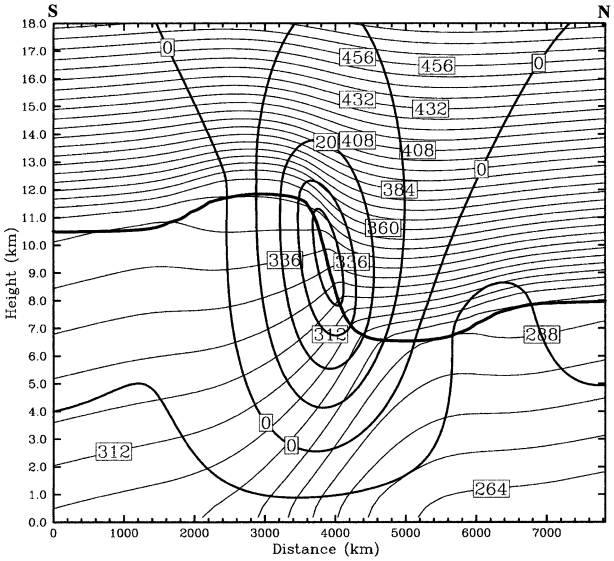

FIG. 1. Vertical cross section of initial potential temperature (thin line, $\Delta = 8$ K) and zonal velocity (thick line, $\Delta = 10$ m s^{-1}) for the initial basic-state jet. The gray thick line denotes the location of the tropopause where potential vorticity equals 1.5 PVU.

b. Initial condition

Assuming the nonlinear balance (Charney 1955) as the underlying balance condition, the initial condition of an idealized two-dimensional (2D) baroclinic jet with a balanced three-dimensional (3D) perturbation is generated for the coarse domain (D1) from the following steps.

- *Step 1.* Following Rotunno et al. (1994, hereinafter RSS94), we first create a zonally invariant baroclinic jet by specifying the geometry of the tropopause, with constant potential vorticity (PV) in both the troposphere [0.4 potential vorticity units (PVU, where 1 PVU $\equiv 10^{-6}$ m^2 s^{-1} K kg^{-1})] and stratosphere (4.0 PVU). The value of 1.5 PVU is used to define the location of the tropopause, which is indicated by the thick dashed line in the meridional cross section of Fig. 1. For more information on the specification of the base state, refer to the appendix in RSS94.
- *Step 2.* The balanced wind and potential temperature fields for the jet, also shown in Fig. 1, are obtained by inverting the PV in the y–z plane. A two-dimensional version of the PV inversion technique developed by Davis and Emanuel (1991) is used. A mean zonal wind of 12.5 m s^{-1} is subtracted from the balanced initial condition to minimize the propagation of the baroclinic jet–front systems, thus ensuring that the

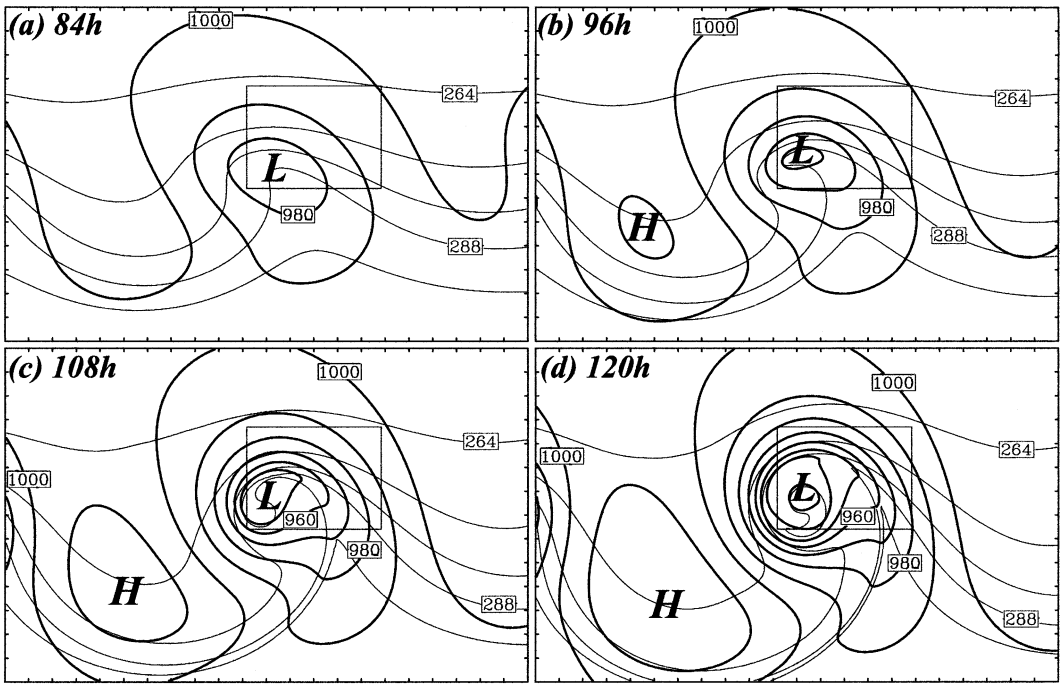

FIG. 2. CNTL simulated surface potential temperature (thin line, $\Delta = 8$ K) and sea level pressure (thick line, $\Delta = 10$ hPa) valid at (a) 84, (b) 96, (c) 108, and (d) 120 h plotted on a subset of D2. The mean pressure gradient used to balance a 12.5 m s^{-1} phase speed reduction was subtracted for the sea level pressure fields. The inner rectangular box denotes the location of Figs. 5–8. The distance between tick marks is 300 km.

features of interest stay far away from the lateral boundaries for all model domains. A uniform north–south horizontal pressure gradient is also added to balance the mean wind speed subtraction.

- *Step 3.* A localized, three-dimensional, balanced perturbation of moderate amplitude is then added to the base state of step 2 to represent the early phase of a typical midlatitude cyclogenesis. Similar to Rotunno and Bao (1996), the perturbation is obtained by specifying a horizontal displacement field and calculating a PV perturbation by multiplying that displacement by the meridional gradient of PV. For more information on the specification of the PV perturbation, refer to Rotunno and Bao (1996, 1057). The PV disturbance is concentrated only at the tropopause level. This PV perturbation is then added to the background PV (step 1) to form the 3D perturbed PV.
- *Step 4.* We then invert the 3D perturbed PV fields from step 3 for the streamfunction and geopotential (and thus wind and temperature) fields, again using the PV inversion technique of Davis and Emanuel (1991).

3. Simulated life cycle of baroclinic waves

Figure 2 shows the evolution and the structure of the surface temperature and sea level pressure at different stages of the baroclinic waves simulated by CNTL plotted on a subset of D2 (Δx, $\Delta y = 30$ km). The mean pressure gradient used to balance the added 12.5 m s^{-1} phase speed of the baroclinic waves was subtracted from the sea level pressure fields. The corresponding evolution and structure of the pressure, potential temperature, and wind fields at 8 km (the level of strongest winds within the baroclinic wave) is shown in Fig. 3. By 84 h, an incipient cyclone has developed out of the initial perturbation to the basic flow with a minimum sea level pressure of ~975 hPa (Fig. 2a). The simulated baroclinic wave has a zonal wavelength of ~4200 km. At 8 km, an elongated jet streak is located upstream of the primary pressure trough but downstream of the pressure ridge. A descending tropopause (Wandishin et al. 2000) and the resultant adiabatic warming begin to build a thermal ridge in the pressure trough region; cooling (thermal trough) is building in the pressure ridge area (Fig. 3a).

At 96 h, the surface cyclone has reached a minimum sea level pressure of ~960 hPa with a ''T bone'' structure and a ''bent back'' warm front (Fig. 2b). At the 8-km level, closed warm and cold centers begin to emerge while the pressure trough and ridge become deeper and stronger; as the jet streak gains strength, its leading edge is also migrating across the pressure trough (Fig. 3b). Since there is no surface friction applied throughout the simulation, the surface cyclone continues to deepen further with a minimum sea level pressure of ~945 hPa at 108 h (Fig. 2c). At 8 km, a closed pressure low forms in the trough region at 108 h and the strengthening jet

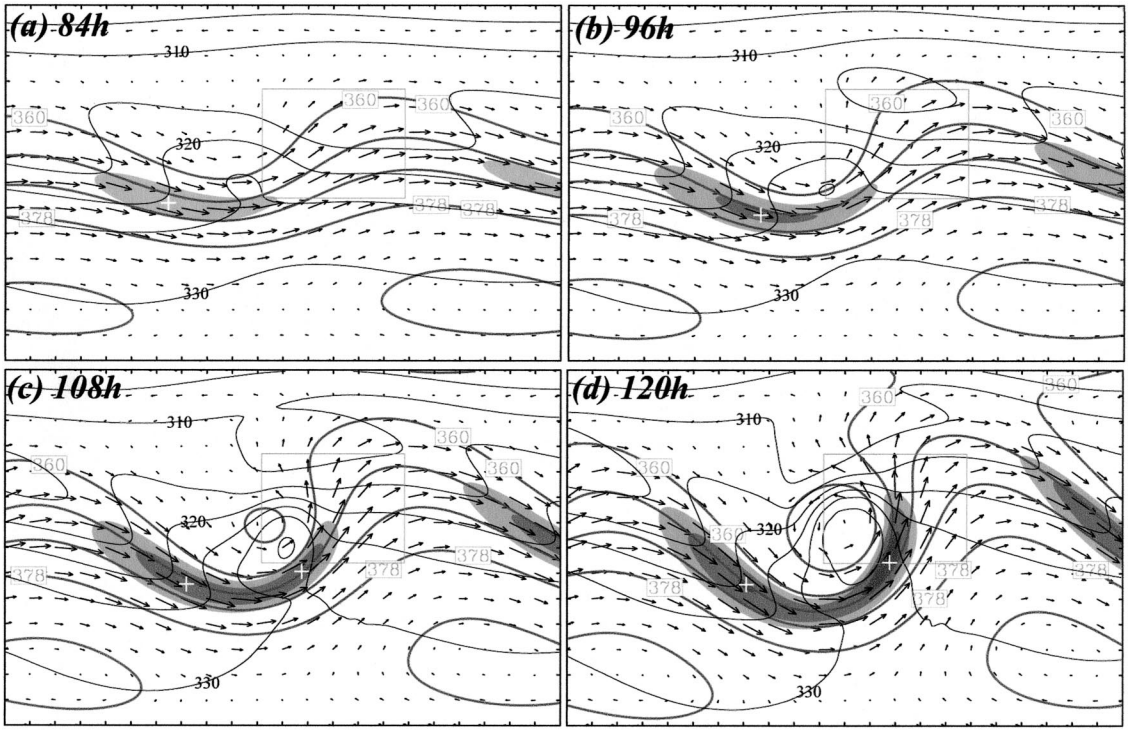

FIG. 3. CNTL simulated 8-km pressure (thick line, $\Delta = 5$ hPa), potential temperature (thin line, $\Delta = 8$ K), and winds (maximum of 50 m s^{-1}, values greater than 40 shaded, $\Delta = 5$ m s^{-1}) valid at (a) 84, (b) 96, (c) 108, and (d) 120 h plotted on the subset of D2 as in Fig. 2. The inner rectangular box denotes the location of Figs. 5–8. The local wind speed maxima are denoted with ''+''. The distance between tick marks is 300 km.

streak reaches the inflection point between upstream trough and downstream ridge; the flow is strongly diffluent ahead of the jet streak (Fig. 3c). At 120 h, the mature cyclone reaches as low as ~930 hPa in sea level pressure with a warm-core structure (Figs. 2d). In the meantime, separated wind speed maxima develop on both sides of the pressure trough; the one downstream of the trough is slightly stronger (Fig. 3d).

The evolution of the potential temperature and pressure at the surface and the jet stream level simulated here is qualitatively similar to the life cycle of a typical extratropical cyclone described by Shapiro and Keyser (1990). In general, the control simulation reproduces the features found in previous primitive-equation simulations of baroclinic waves; these features are, in turn, fairly realistic (see, e.g. Rotunno and Bao 1996). Hence we use these simulations as a basis in which to examine the generation of mesoscale gravity waves.

4. Characteristics of simulated mesoscale gravity waves

a. Overview

We first examine the evolution of the horizontal velocity divergence at 13 km during the baroclinic wave life cycle (Fig. 4). Figure 4 is plotted on the same subset of D2 as in Figs. 2–3. At 84 h (Fig. 4a), the horizontal divergence displays a classical pattern for developing baroclinic waves with convergence/descending flow upstream of the pressure trough and divergence/ascending flow ahead of the trough (Keyser and Shapiro 1986). As the baroclinic wave intensifies over the next 12 h, mesoscale variations (largely gravity wave activity) with different wavelengths (~100–500 km) appear in both the convergent and divergent parts of the flow; the intensity of the divergence also increases significantly during this period (Fig. 4b). At 108 h, mesoscale waves with distinct wavelength ~150 km emerge from the original divergent center (Fig. 4c), right after the juxtaposition of the surface fronts (Fig. 2c) and the upper-level jet streak (Fig. 3c). While intensifying with the background baroclinic wave, these mesoscale waves persist for the next 12–24 h with little change in characteristics (Fig. 4d) while animations indicate that they preserve their individual identity.

Besides these mesoscale waves, which are clearly associated with the upper-level jet–front system (details below), at 120 h or even earlier, mesoscale waves are also noticeable to the south of the jet stream and also in the convergence region upstream of the pressure trough (Figs. 4c,d). Mesoscale waves in both of these regions can be traced back to the surface frontal boundaries where the mean flow allows vertical propagation. These waves that originated from the surface fronts tend

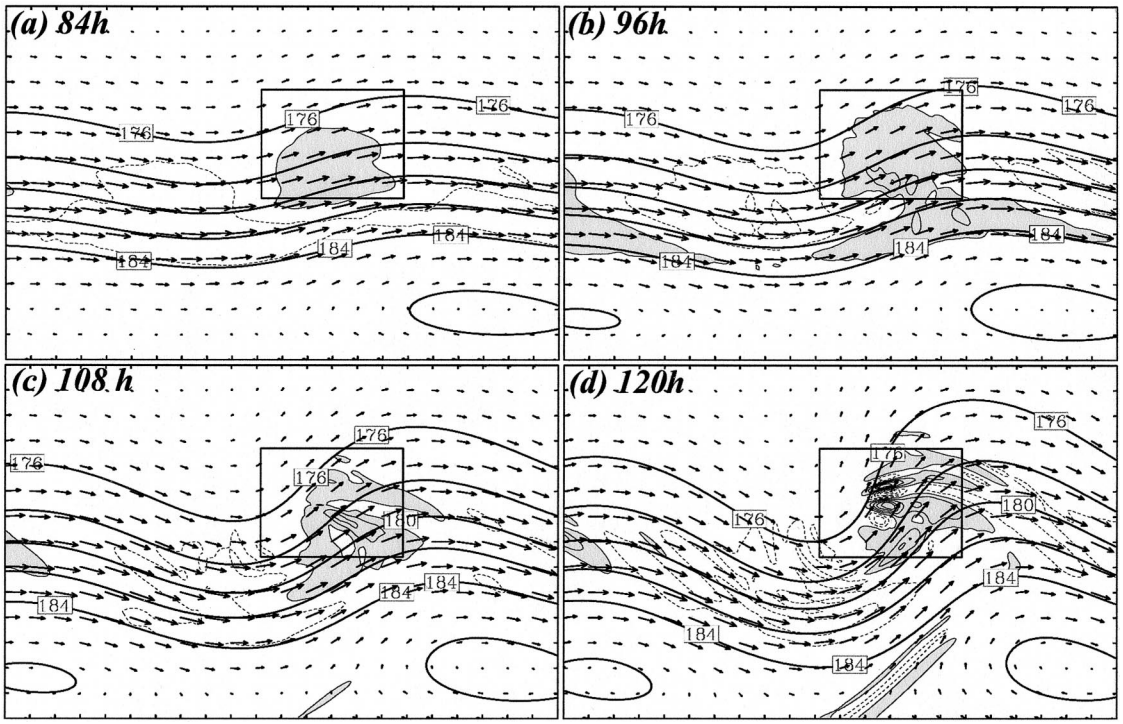

FIG. 4. CNTL simulated 13-km pressure (thick line, $\Delta = 2$ hPa), horizontal divergence (thin line; solid and shaded, positive; dashed, negative; $\Delta = 2 \times 10^{-6}$ s^{-1}), and wind vectors (maximum of 25 m s^{-1}) valid at (a) 84, (b) 96, (c) 108, and (d) 120 h plotted on the subset of D2 as in Figs. 2–3. The inner rectangular box denotes the location of Figs. 5–8. The distance between tick marks is 300 km.

to have shorter horizontal wavelengths (<100 km), and their intensity and wavelength are determined largely by the model resolution and diffusion according to the sensitivity experiments described in the next section. These shorter waves are similar to those examined by Snyder et al. (1993), and will not be examined further in the current study.

Furthermore, the inertia–gravity waves with wavelength 600–1000 km simulated by OD95 are absent from our high-resolution simulations, or at least not as easily identifiable compared to other significant smaller-scale (mesoscale) gravity wave activity.

b. Incipient mesoscale gravity waves

Evolution of the vertical velocity and potential temperature in the inner rectangular box denoted in Figs. 2–4, where the mesoscale waves of interest are confined, and along the vertical cross section approximately perpendicular to the wave fronts, is examined in detail for the wave structure and characteristics (Figs. 5–6). The incipient gravity wave (a vertical velocity ridge, named wave 1 or W1) is first clearly identifiable in the vertical velocity field along the cross section between 11 and 16 km at 102 h, tilting upstream (Fig. 5c); a weak signal of W1 is also vaguely seen in the vertical velocity field at 13 km (Fig. 5a). Wave 1 is directly above the exit region of the upper-tropospheric jet streak (~8–9 km; Figs. 2b,c and 3b,c). Flow configuration in this region has been found to be suitable for mesoscale gravity wave activity by UK87. Even though W1 is also located in a region above the surface front, no direct connection to the surface frontal waves has been detected after careful examination of other model variables (not shown). This is not to say that the surface front is a nonfactor—it is an essential part of the baroclinic wave life cycle coupling closely with the upper-level jet–front system. In particular, it contributes to the intensification and curvature of the upper-level jet streak and the flow imbalance in general, which could be crucial in wave generation (details in section 6). At 108 h, while W1 greatly amplifies in both the vertical and horizontal plots, wave 2 (W2) emerges in the vertical velocity field ~150–200 km ahead of W1 (Figs. 5b,d). In the meantime, wave-induced fluctuations of potential temperature also become visible with a positive (negative) potential temperature perturbation approximately a quarter of a horizontal wavelength upstream (downstream) of the vertical velocity maximum (Fig. 5b).

c. Mature mesoscale gravity waves

Downward motions associated with the developing gravity waves (W1 and W2) develop rapidly between 108 and 114 h and reach an amplitude comparable to (or even stronger than) the upward motions, at 114 h

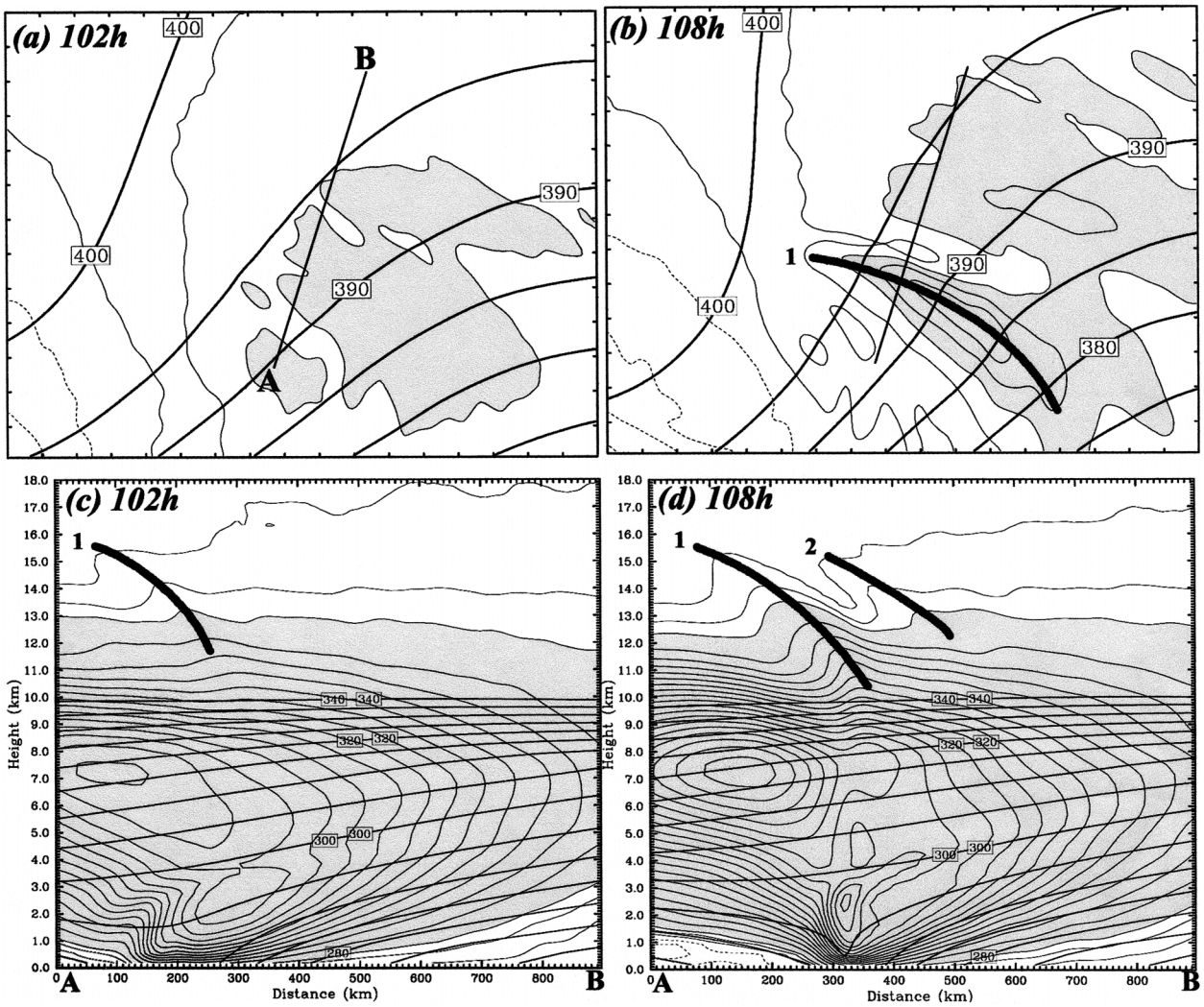

FIG. 5. CNTL simulated potential temperature (thick line, $\Delta = 5$ K) and vertical velocity (solid, positive; dashed, negative; $\Delta = 2 \times 10^{-3}$ m s^{-1}; values $>5 \times 10^{-3}$ m s^{-1} shaded) at the 13-km level valid at (a) 102 and (b) 108 h, and along the cross section AB valid at (c) 102 and (d) 108 h plotted on a subset of D3 with its location denoted in Figs. 2–4. The straight line AB in (a) and (b) denotes the location of the cross section in (c) and (d). Contours of potential temperature greater than 340 K are generally flat but dense in the stratosphere and were thus not plotted in (c) and (d). The distance between tick marks in (a) and (b) is 100 km.

(Figs. 6a,c). At 13 km, the wave-induced potential temperature perturbations reach an amplitude of ~0.5–1.0 K (Fig. 6a). Also at 13 km, the gravity waves curve further to the cyclonic side of the flow and propagate northward. At 114 h, another vertical velocity maximum (wave 3 or W3) begins to appear ahead of the leading edge of W2 in the cross section (Fig. 6c). The distance between W2 and W3 is shorter than that between W1 and W2 at this time. At 120 h, W3 develops further with significant potential temperature fluctuations; the averaged distance between W2 and W3 is ~150 km at the 13-km level (Figs. 6b,d). In the meantime, W1 deforms with horizontal wavelength above 12 km expanding with height (Fig. 6d), either due to local changes in the background flow or due to changes in the forcing. As the baroclinic wave further intensifies, more waves will be subsequently initiated ahead of the leading edge of the wave packet with their path curving further leftward (not shown).

d. Wave characteristics

As noted above, the potential temperature anomalies associated with these mesoscale waves lag a quarter of a horizontal wavelength behind the vertical velocity maxima, characteristic of gravity waves propagating freely against a background flow. In this subsection, we will examine in detail the characteristics, propagation and dispersion relationship of these mesoscale waves.

At 13 km, the mean ground-based propagation speed of the waves (C), averaged from 111 to 117 h, is ~6.0 m s^{-1} northward. During the same period, the average

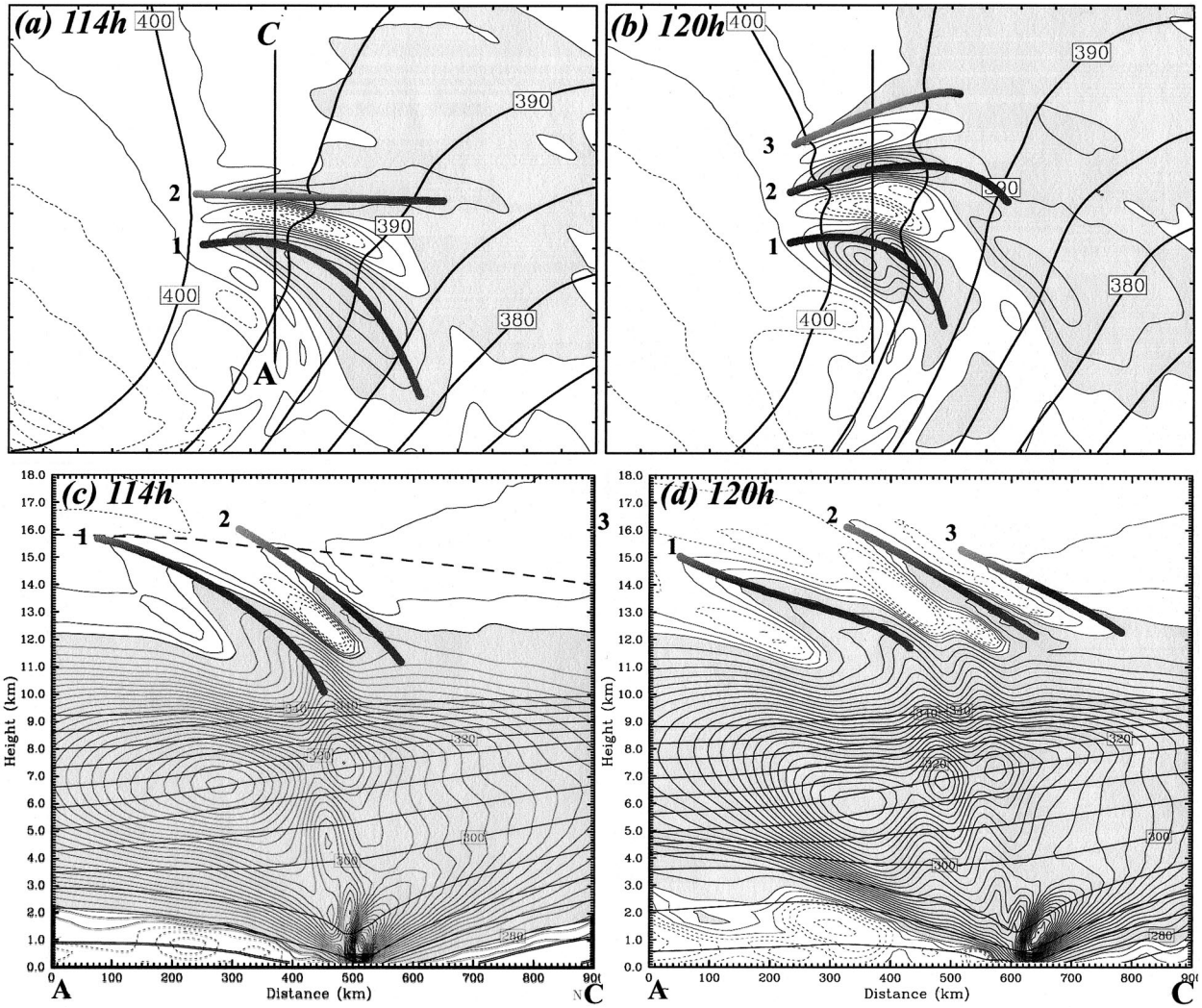

FIG. 6. As in Fig. 5a but for (a) 114 and (b) 120 h and in Fig. 5c but for (c) 114 and (d) 120 h along cross section AC denoted in (a). The thick dashed line in (c) indicates the location of a critical level.

horizontal and vertical wavelength (L_x and L_z) of the gravity waves (evaluated as the horizontal and vertical distance between W1 and W2 along the cross section AC at around 13 km) is approximately 150 and 2.5 km, respectively (Figs. 6b,d). Since the mean wind speed (U) at 13 km along the cross section is ~14.0 m s^{-1}, the mean intrinsic phase speed (C_i) in the simulation is 8 m s^{-1} southward.

The dispersion relationship of a propagating hydrostatic ($m^2 \gg k^2$) gravity wave in a rotating atmosphere is

$$C_i = \frac{\omega_i}{k} = \sqrt{\frac{f^2}{k_2} + \frac{N^2}{m^2}}. \quad (1)$$

Assuming a lower-stratosphere Brunt–Väisälä frequency (N) of 0.02 s^{-1}, $L_x = 150$ km, and $L_z = 2.5$ km, the dispersion relation gives the intrinsic phase speed (C_i) to be 8.2 m s^{-1}. This derived value compares well with the phase speed of 8 m s^{-1} observed in the model. Thus, the model waves are consistent with linear gravity wave theory.

The vertical tilting and the intrinsic phase speed of the waves imply the wave energy is propagating upward. The vertically propagating gravity waves are dissipated between 16–18 km where they encounter a critical level, that is, when the background wind speed equals the wave phase speed (Fig. 6c). Subsequently these waves are quickly absorbed by model diffusion. However, proper treatment of wave dissipation/breaking when the gravity waves approach the critical level cannot be resolved by the current model resolution. Also, horizontal variations in the background flow result in horizontally inhomogeneous wave characteristics.

The processes that determine the characteristics of the waves in the simulations are unknown. Numerous sensitivity experiments (not shown) demonstrate that the wave characteristics are very sensitive to different configurations of the initial baroclinic jet. Longer (shorter)

waves with smaller (larger) intrinsic frequencies are found to be simulated in experiments with weaker (stronger) initial jets and slower (faster) growth of the baroclinic waves. For the waves discussed above, $f^2/k^2 \ll N^2/m^2$, so the Coriolis force is only marginally important in controlling the properties of these mesoscale waves. The Coriolis force will become increasingly more important to the gravity waves when the wavelength increases. This could partially contribute to the dramatic difference in the wavelength between the current study and that of OD95 because a much smaller growth rate is used in their simulations.

In summary, a packet of mesoscale gravity waves with a predominant horizontal wavelength of about 150 km lasting more than 24 h is simulated during the life cycle of baroclinic waves. The wavelength and frequency of the simulated gravity waves are consistent with past observational studies (e.g., UK87; Fritts and Nastrom 1992; Thomas et al. 1999), but differs significantly from those simulated by OD95. The gravity waves appear to be originated from the upper-tropospheric jet–front system and in the left exit region of the upper-level jet streak, which has been conceptualized to be suitable for mesoscale gravity wave activity by UK87. Generating mechanisms of the mesoscale gravity waves will be discussed in section 6.

5. Sensitivity to model resolution

a. Vertical resolution: EXP120L

Insufficient and inconsistent model resolutions have been found to produce spurious gravity waves in numerical models (e.g., Lindzen and Fox-Rabinovitz 1989; Snyder et al. 1993). To determine the adequacy of the model resolution and verify whether the gravity waves simulated in CNTL are physically generated, two high-resolution experiments (EXP120L and EXP3.3KM, respectively) have been performed.

EXP120L is the same as the CNTL experiment, with three model domains, except that the vertical resolution of the model is doubled. In EXP 120L, 120 vertical layers with grid spacing of ~180 m have been used instead of 60 layers with ~360 m spacing used in CNTL. Except for small differences in the gravity waves associated with the surface fronts, EXP120L produces nearly identical mesoscale gravity waves (not shown) associated with the upper-tropospheric jet–front systems to those discussed in the previous section. It is thus concluded that the 360-m vertical grid spacing matches sufficiently to the 10-km horizontal grid spacing used in CNTL.

b. Horizontal resolution: EXP3.3KM

To examine the model sensitivity to horizontal resolution, EXP3.3KM was performed exactly the same as in the EXP120L but a fourth domain (D4) with horizontal grid spacing of 3.3 km was nested within D3. Here D4 covers an area of 1833 km in the *x* direction and 1333 km in the *y* direction centered around (15 218 km, 4636 km) of D1, which is a slightly larger area than the inner box denoted in Figs. 2–4. Thus, the horizontal and vertical grid spacing of EXP3.3KM is 3.3 km and 180 m, respectively. Domain D4 is initialized at 96 h and one-way nesting is applied for the boundary conditions of D4 (because of limited computing resources).

Figure 7 shows the vertical velocity and potential temperature at 13 km and along the cross section at 114 and 120 h. To examine the results from EXP3.3KM on a similar scale to CNTL, the results are smoothed using a nine-point smoother repeatedly. Nevertheless, comparing against results from CNTL (Fig. 6), the smoothed vertical motion field from EXP3.3KM (Fig. 7) still displays stronger intensity and more smaller-scale variability. Except for a much stronger surface frontal gradient simulated in EXP3.3KM, the difference in potential temperature in the upper troposphere and stratosphere between CNTL and EXP3.3KM is rather small. Moreover, the mesoscale gravity waves (e.g., W1, W2, and W3) in CNTL are produced in this extremely high-resolution experiment with nearly identical timing, origination, and wave characteristics (i.e., horizontal and vertical wavelength, propagation speed, and frequency). There are also some noticeable differences between the two simulations: 1) the intensity of the upper-tropospheric and stratospheric mesoscale gravity waves are stronger in EXP3.3KM, especially at the leading edge and cyclonic side of the wave packet (including W1, W2, and W3); 2) the much stronger surface frontal gradient in EXP3.3KM apparently has forced circulations/waves that directly interfere with the upper wave packets (Figs. 7b,d). The wave interference from the surface front is only vaguely seen in the CNTL simulation (Fig. 6d). On the other hand, diagnosis shows that the horizontal scale (wavelength) of gravity waves associated with the surface fronts decreases greatly in the higher resolution simulations because of a much narrower frontal zone with a stronger temperature gradient at the surface (not shown), much like those found by Snyder et al. (1993) on the 2D frontal collapse. Comparison between CNTL and EXP3.3KM provides further evidence that the mesoscale gravity waves (W1, W2, W3, etc.) originated from the upper-level jet–front system are adequately resolved in CNTL. Also, these upper-level waves' initiation and characteristics are not a direct consequence of the surface frontogenesis and its sensitivity to resolution, although EXP3.3KM also suggests that it is possible for the surface frontally forced waves to penetrate/propagate into the stratosphere. The sensitivity to the grid resolution is qualitatively similar to the simulations of an observed gravity wave event studied in Zhang et al. (2003).

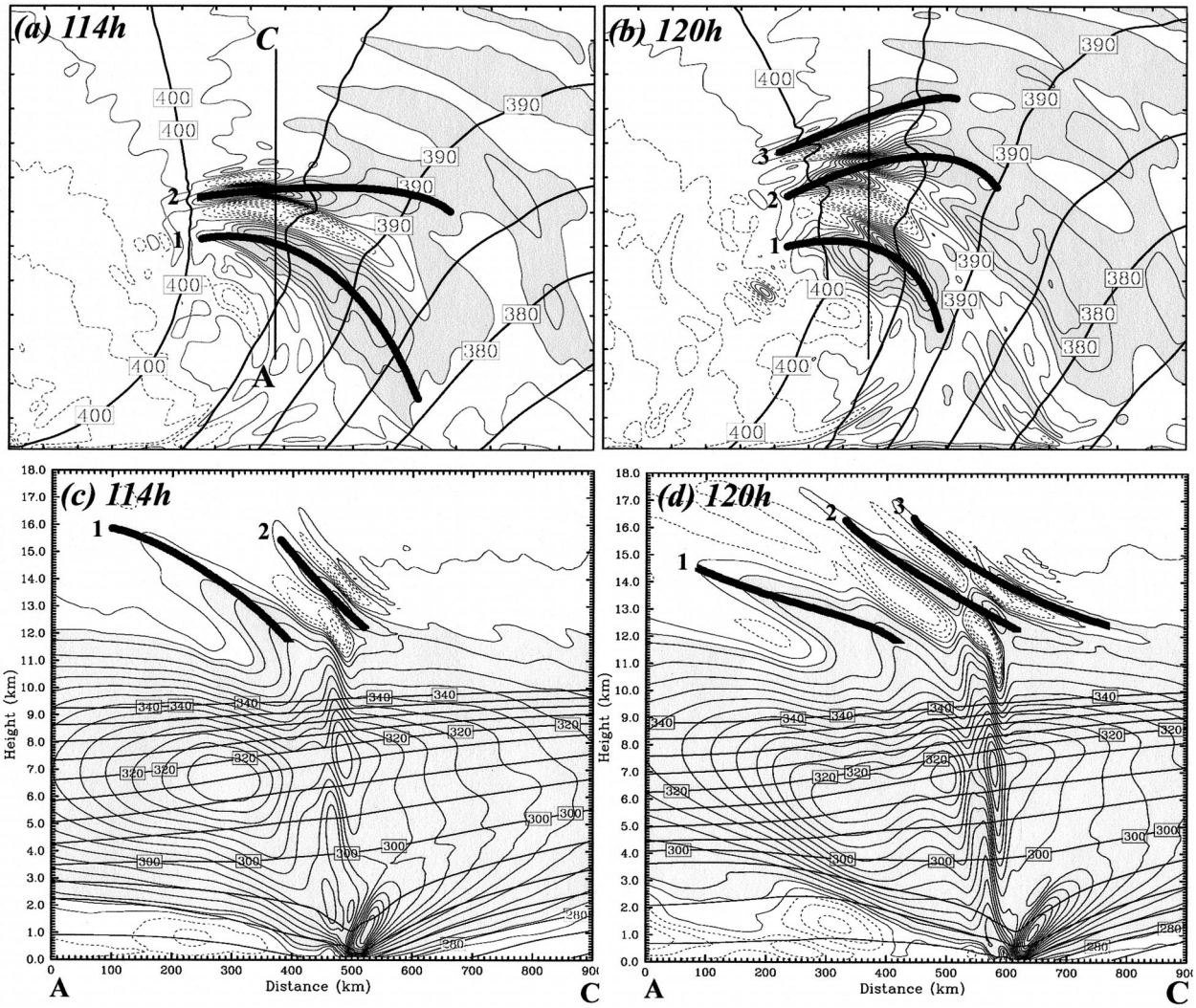

FIG. 7. As in Fig. 6 but for experiment EXP3.3KM plotted on a subset of D4 after smoothing.

c. Horizontal resolution: EXP30KM

A lower-horizontal resolution experiment (EXP30KM) was also performed exactly the same as for the CNTL experiment but with only two model domains (D1 and D2). Figure 8 shows the vertical velocity and potential temperature at 8 km and along the cross section at 114 and 120 h plotted on the 30-km domain (D2). In this experiment mesoscale gravity waves are found to be simulated in this lower resolution experiment with similar timing and location in comparison to the previous simulations. However, the horizontal wavelength of these waves is slightly larger. It is likely that the gravity waves simulated in CNTL and EXP3.3KM cannot be adequately resolved in EXP30KM because they have a wavelength of ~150 km: only ~5 times the horizontal grid spacing. Nevertheless, this lower-resolution experiment (EXP30KM) simulates the fundamental dynamics leading to the initiation of the mesoscale gravity waves quite well in comparison to the higher-resolution simulations.

d. Horizontal diffusion: "DIFFUS"

As is standard in MM5, the control simulation employs a fourth-order horizontal diffusion throughout the model domain except for the grid points near the boundaries of the coarsest domain where a second-order horizontal diffusion is applied. No vertical diffusion is used. The diffusion coefficient is determined by the horizontal grid spacing, time step, and the horizontal deformation. The standard treatment of horizontal diffusion in MM5 can be found in Grell et al. (1994, p. 37). In an attempt to distinguish the gravity waves generated at the upper troposphere from those originated at the surface fronts, we performed an experiment exactly the same as CNTL except that an additional second-order horizontal diffusion was applied to the lower troposphere below 5 km (DIFFUS). This additional second-order diffusion was four times its default value at the surface but gradually decreased to zero at 5 km. A similar experiment has been previously used by OD95 except that they

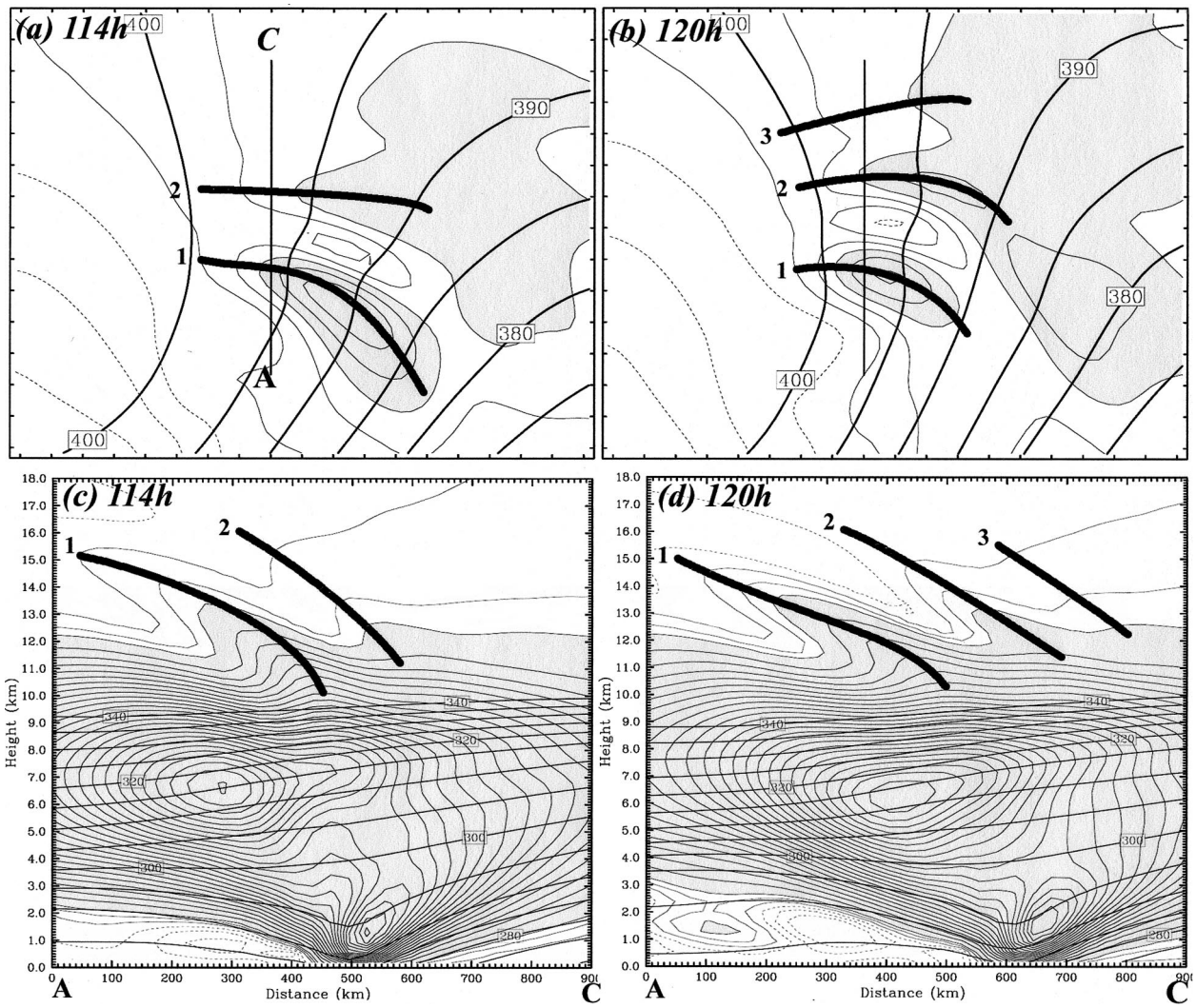

FIG. 8. As in Fig. 6 but for experiment EXP30KM plotted on subset of D2.

applied an additional six-order diffusion to divergence only in the lower troposphere (their page 3702).

The additional low-level second-order diffusion is very effective in weakening the surface frontal gradient as well as removing gravity waves directly forced by the fronts near the surface. Because of the strong baroclinic coupling between the surface and upper-level front (jet streak), the development of the jet streak in the upper troposphere is significantly delayed as well. Subsequently, the onset of the incipient mesoscale gravity waves was also delayed by ~36 h. However, albeit slightly weaker in magnitude, mesoscale gravity waves with similar characteristics (wavelength, frequency, and phase speed) to those in CNTL are initiated in a similar location (left exit region) relative to the upper-level jet–front system (Fig. 9 versus Fig. 5). Without the interference of the frontally forced waves originated from the surface, the mesoscale waves radiated from the upper jet–front system in DIFFUS preserve their individual identity and strength even longer than those simulated in CNTL (not shown). Meanwhile, the mesoscale waves to the south of the jet stream and also in the convergence region upstream of the pressure trough (Fig. 4d) are both absent in DIFFUS (not shown). This experiment further demonstrates that the initiation of the upper-level mesoscale gravity waves in CNTL is not an artifact of model resolution or a function of the strength of the surface fronts. It also provides further evidence that these mesoscale waves are not directly generated at or near the surface fronts.

6. Discussions on flow imbalance and wave initiation

In this section we attempt to determine the governing dynamics leading to the generation of the mesoscale gravity waves seen in the simulations. Since the bulk Richardson number in the upper troposphere never falls

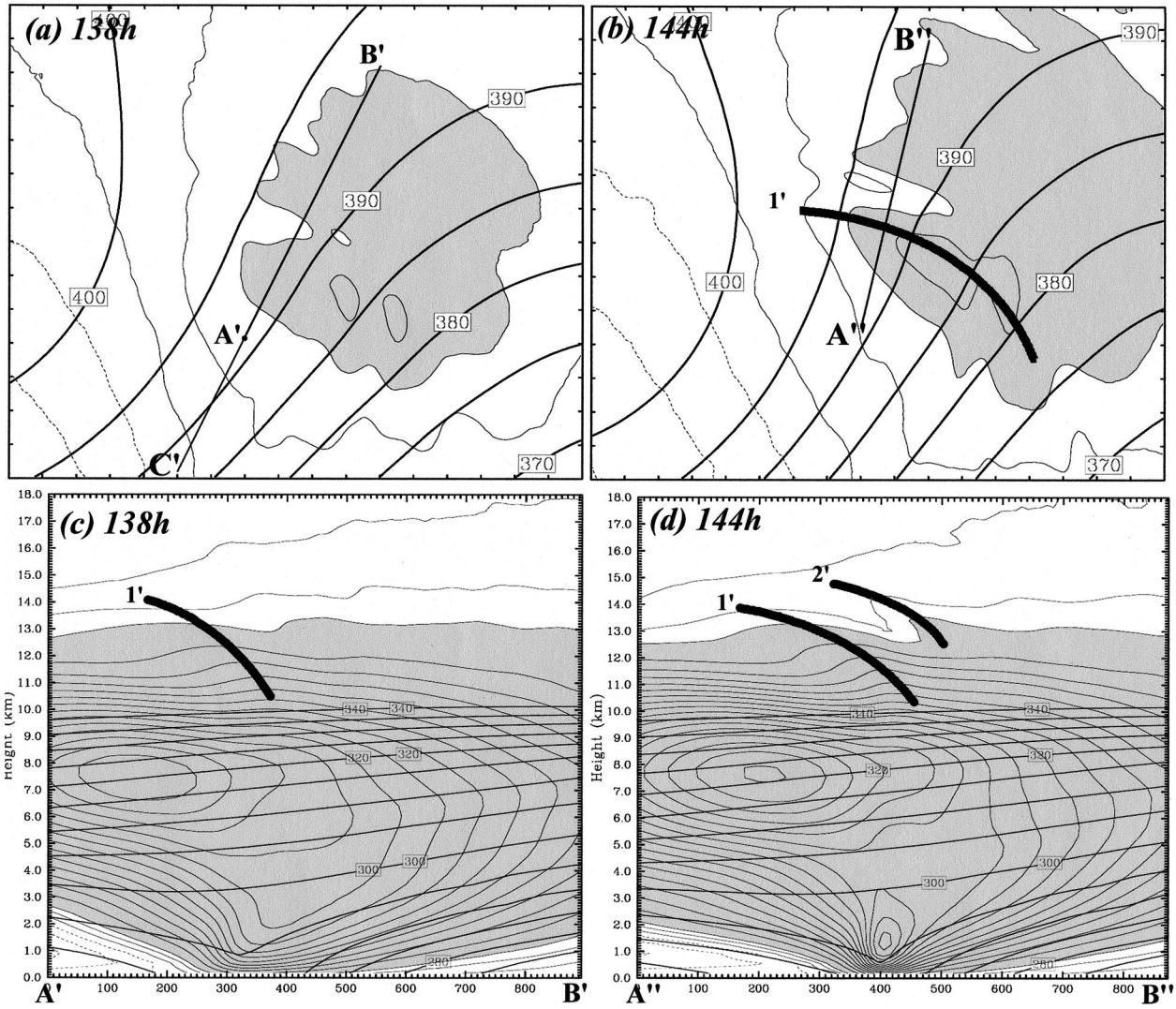

FIG. 9. As in Fig. 5 but for experiment DIFFUS at (a),(c) 138 and (b),(d) 144 h. Lines A′B′ and A″B″ denote the location of cross sections plotted in (c) and (d), respectively. Line C′B′ denotes the location of the cross section plotted in Fig. 12.

below 1.0 throughout the CNTL simulation, wave forcing due to shear instability (e.g., Dunkerton 1997) can be ruled out. However, the simulated gravity waves are originated from the left exit of the upper-level jet streak, consistent with the conceptual model of UK87, and it is therefore possible that these mesoscale waves are generated through geostrophic adjustment associated with an unbalanced upper-tropospheric jet–front system.

Geostrophic adjustment is widely believed to be one of the most prevalent wave generation mechanisms (Rossby 1938; Cahn 1945; Blumen 1972; Kaplan and Paine 1977; Van Tuyl and Young 1982; Keyser and Shapiro 1986; UK87; Koch and Dorian 1988; OD95; Kaplan et al. 1997; Zhang et al. 2001). The fundamental concept behind the geostrophic adjustment hypothesis is the existence and the definition of a balanced state. Imbalance is defined in terms of the extent to which the flow departs from the balanced state. The balanced state (condition) must be physically realizable in the sense that static instability, inertial instability, the related symmetric instabilities and gravity waves are all absent (Hoskins et al. 1985). The nonlinear balance, which is constrained by PV, is generally believed to be a more appropriate balance than geostrophy for the real atmosphere, especially at the mesoscale (e.g., Charney 1955; Gent and McWilliams 1982; Hoskins et al. 1985; Allen 1991; Davis and Emanuel 1991; Raymond 1992; McIntyre and Norton 2000; Zhang et al. 2000). In this case, ''balance adjustment'' is more general (and may be more appropriate) than ''geostrophic adjustment'' and describes the process in which the atmospheric flow adjusts toward the nonlinear balance (or any appropriate balance), and thus will be used in the discussion hereafter.

As in Zhang et al. (2001), the flow imbalance is first

evaluated through diagnosis of the residual of the nonlinear balance equation (ΔNBE):

$$\Delta\text{NBE} = 2J(u, v) + f\varsigma - \alpha\nabla^2 P, \qquad (2)$$

where u, v, P, f, α, and ς are the zonal and meridional velocities, pressure, Coriolis parameter, specific volume, and relative vorticity, respectively. The Jacobian term $J(u, v) = \partial u/\partial x \times \partial v/\partial y - \partial v/\partial x \times \partial u/\partial y$. In essence, the *magnitude* of ΔNBE indicates the *degree of imbalance*; that is, it quantifies the deviation of the flow from the nonlinear balance state. The residue of the nonlinear balance equation is also a first-order approximation for the tendency of the horizontal divergence.

As in the original geostrophic adjustment hypothesis, it is hypothesized that a large degree of imbalance will result in *adjustment toward balance* and thus leads to the generation of gravity waves. Using the PV inversion technique with the nonlinear balance as the underlying balance condition, Zhang et al. (2001) found that a positive ΔNBE anomaly corresponds closely to a positive geopotential height (or positive pressure) anomaly because the vorticity (or streamfunction) in the region of imbalance usually remains nearly unchanged (and thus nearly balanced) before and after the PV inversion. Because gravity waves are also unbalanced motions, they can also be reflected (and thus identified) in the ΔNBE field. However, this could also limit the distinction between gravity waves and imbalance when the gravity wave response reaches an amplitude comparable to the imbalance forcing.

The evolution of ΔNBE at 8 km and along a cross section is plotted in Figs. 10–11 (Fig. 10 is plotted on the same subset of D2 as in Figs. 2–4). By the experimental design discussed in section 2b, at 0 h, the initial 2D baroclinic jet and the 3D perturbation are exactly balanced with ΔNBE equal zero; the developing baroclinic wave (including the upper-level jet streak and surface fronts) evolves mostly under balanced (or quasi-balanced) dynamics with very small (albeit growing) ΔNBE for the first 60 h of simulation (not shown). At 78 h, a distinct ΔNBE maximum of about 0.9×10^{-9} s^{-2} begins to develop ahead of the pressure trough and in the left exit region of the jet streak at 8 km (Fig. 10a). Vertically, this ΔNBE maximum is located in the vicinity of the folding tropopause (which is essentially an upper-level front) (Fig. 11a). Both the horizontal and vertical plots suggest that the imbalance is intimately associated with and may be produced by the upper-level jet–front system (Figs. 10a, 11a). A secondary maximum of ΔNBE can also be found at ~2 km in the cross section (Fig. 11a), which can be traced back to the primary maximum near the tropopause at earlier times (not shown).

As the baroclinic wave and the 8-km jet streak strengthen gradually, ΔNBE increases and thus the flow becomes more unbalanced (Figs. 10b, 11b). At 90 h, it reaches a maximum of $\sim 1.8 \times 10^{-9}$ s^{-2} at 8 km (Fig. 10c). Vertically, downstream of the ΔNBE maximum, weak negative maxima of ΔNBE begin to develop both in the troposphere and in the lower stratosphere (Fig. 11c). These negative ΔNBE maxima have the signature of weak propagating gravity waves from the imbalance maximum even though distinct gravity waves are hardly identifiable in the vertical motion fields at this time. This incipient gravity wave activity ahead of the primary imbalance maximum becomes more evident both horizontally and vertically at 96 h; in the meantime, the leading edge of the maximum deforms into a nearly straight line with sharper gradient of ΔNBE (Figs. 10d, 11d). By 102 h, as the leading edge of the jet streak migrates across the inflection line between the upstream trough and the downstream ridge, the ΔNBE reaches a magnitude of $\sim 3.8 \times 10^{-9}$ s^{-2} at 8 km (Fig. 10e), more than quadrupled over the past 24 h. In the meantime, a fairly strong negative ΔNBE maximum and a weak positive ΔNBE maximum in the lower stratosphere develops downstream of the primary ΔNBE maximum. This pattern corresponds directly to the incipient upward propagating gravity wave (W1), which can be clearly identified in the vertical motion field at this time (Fig. 5c). At 108 h (Figs. 10f, 11f) and beyond, the imbalance associated with the primary jet streak and the gravity waves continues to gain strength while preserving their identity.

By removing the complications associated with the balance fields (e.g., vertical motion fields include both balanced and unbalanced motions as well as gravity waves.), ΔNBE not only signals the incipient gravity waves earlier in time, it also indicates that the mesoscale gravity waves that originated from the upper-tropospheric jet–front system extend farther below the tropopause (Fig. 11f) than is indicated by the vertical motion fields (e.g., Fig. 5c). The better and earlier detection of the gravity waves with the diagnosis of ΔNBE is best seen in examining its evolution in a cross section from DIFFUS (Fig. 12). Figure 12 was drawn along the same cross section of Fig. 9c (A′B′) but extends farther to the lower left of the model domain (C′B′). As was discussed in section 5d, only a very weak mesoscale wave signal was seen in the vertical motion fields (~10–14 km) at 138 h (Fig. 9c); at the same time, ΔNBE shows several well-defined gravity waves extending from the middle troposphere to the stratosphere ahead of the imbalance maximum (Fig. 12d). Indeed, these gravity waves can be easily identified as early as 126 h (Fig. 12b), more than 12 h earlier than using the vertical motion fields. Figure 12b also demonstrates unambiguously that mesoscale gravity waves can appear aloft without any significant imbalance or corresponding wave signal at the surface. In addition, by examining the ΔNBE of another cross section in DIFFUS (Figs. 13c,d) with orientation and timing with respect to the jet streak similar to those in CNTL (Figs. 11d,f), the surface-originated gravity waves (refer to section 4a), especially those between 500–1000 km in distance in the lower troposphere. Figure 13 also further demon-

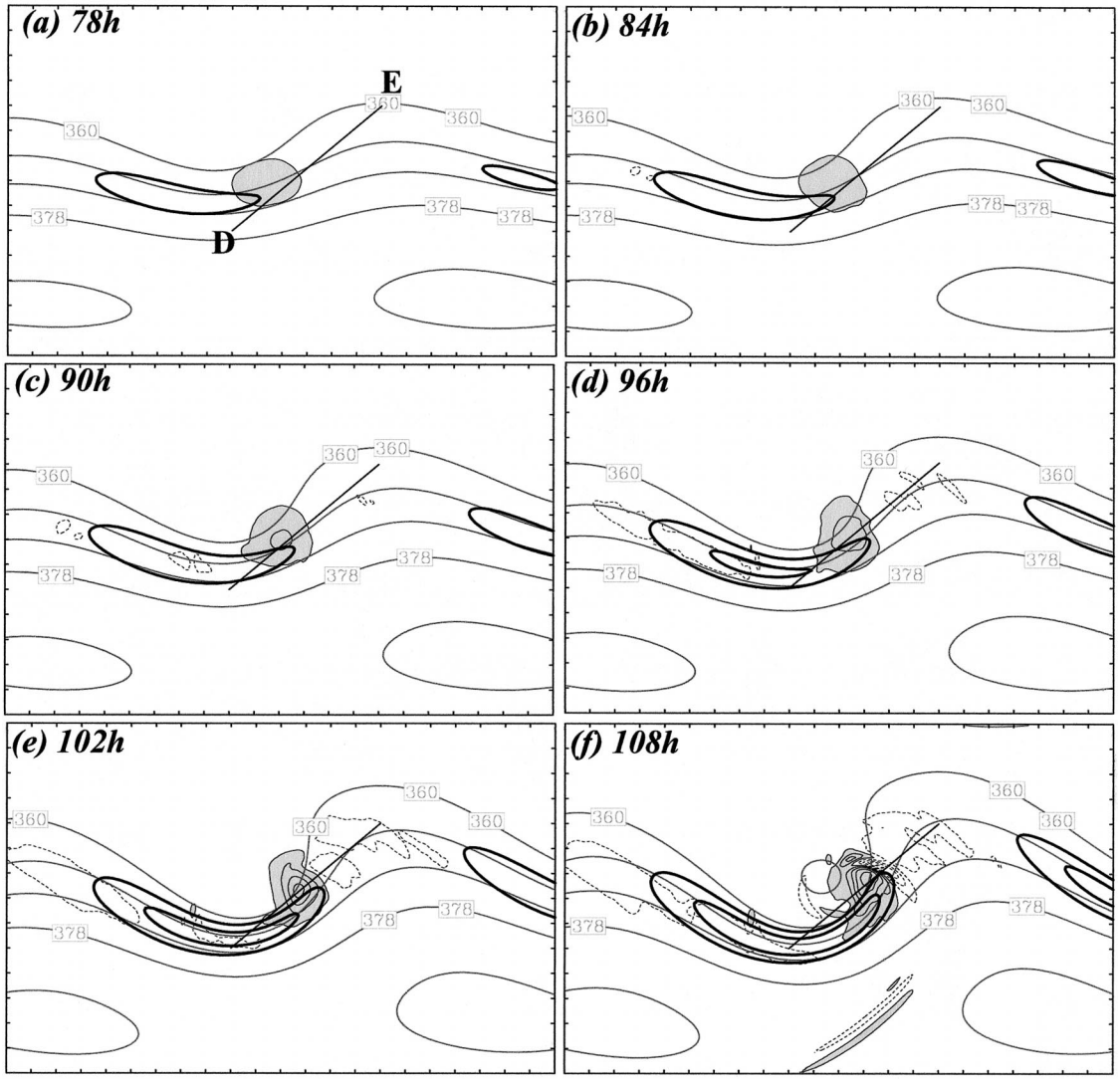

FIG. 10. CNTL simulated 8-km pressure (thick line, $\Delta = 4$ hPa), the residual of the nonlinear balance equation (shaded, solid, positive; dashed, negative; $\Delta = 1 \times 10^{-9}$ s^{-2}), and wind speed over 40 m s^{-1} (bold contours, $\Delta = 5$ m s^{-1}) valid at (a) 78, (b) 84, (c) 90, (d) 96, (e) 102, and (f) 108 h plotted on the subset of D2 as in Figs. 2–4. The straight line DE denotes the location of the cross section plotted in Fig. 11. The distance between tick marks is 300 km.

strated that the development of the imbalance associated with the upper-level jet streak and the subsequent onset of the incipient mesoscale gravity waves are similar to those in CNTL except for a 36-h delay.

From the diagnosis of ΔNBE, there is a strong indication that the primary imbalance aloft acts as a continuous but increasing forcing, which sustains and strengthens the upward propagating gravity waves in the stratosphere (Figs. 10f, 11f). More frequent plots of the ΔNBE field in the cross section as in Fig. 11 and their animations also indicate a downward radiation and propagation of gravity waves from the ΔNBE maximum. Because they are hardly distinguishable from the massive larger-scale balanced updraft and from the gravity waves associated with the surface fronts (Figs. 5–6), their characteristics will not be analyzed in detail in the current study. Gravity waves generated through geostrophic adjustment have been found to propagate both upward and downward from an unbalanced jet streak in numerical simulations by Fritts and Luo (1992, e.g., their Fig. 10) and in an observational study by Thomas et al. (1999).

Figures 10–11 not only demonstrate the usefulness of using ΔNBE as an imbalance indicator to predict the timing and location of mesoscale gravity wave generation, they also give further evidence that the mesoscale gravity waves are likely to be generated through the adjustment of imbalance, that is, balance adjustment. However, in the original framework of geostrophic adjustment (e.g., Rossby 1938; Cahn 1945), which was

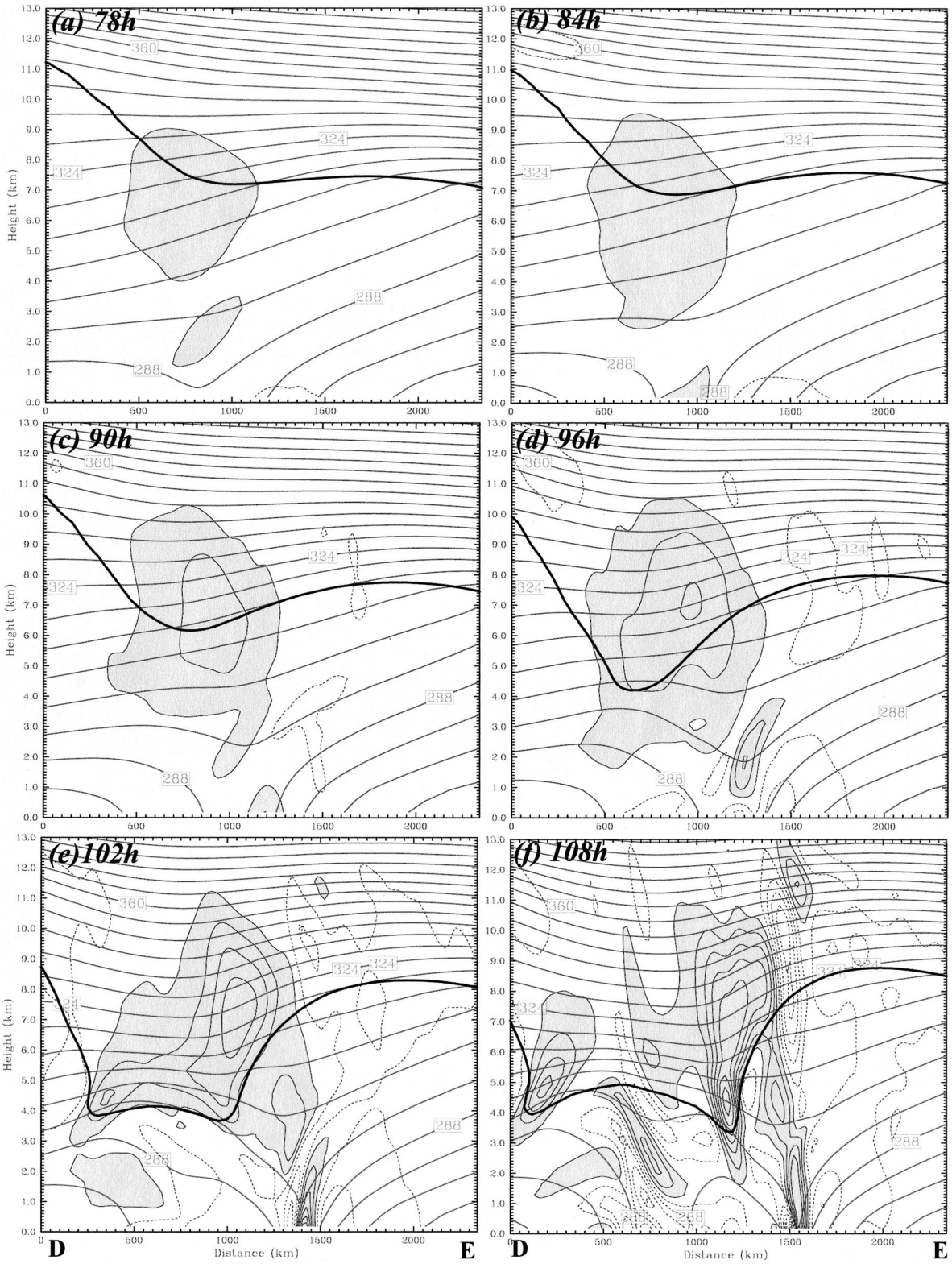

FIG. 11. CNTL simulated potential temperature (thick line, $\Delta = 5$ K) and the residual of the nonlinear balance equation (solid, positive; dashed, negative; $\Delta = 1 \times 10^{-9}$ s^{-2}) and valid at (a) 78, (b) 84, (c) 90, (d) 96, (e) 102, and (f) 108 h along cross section DE plotted on D2. The bold curve denotes the location of dynamic tropopause.

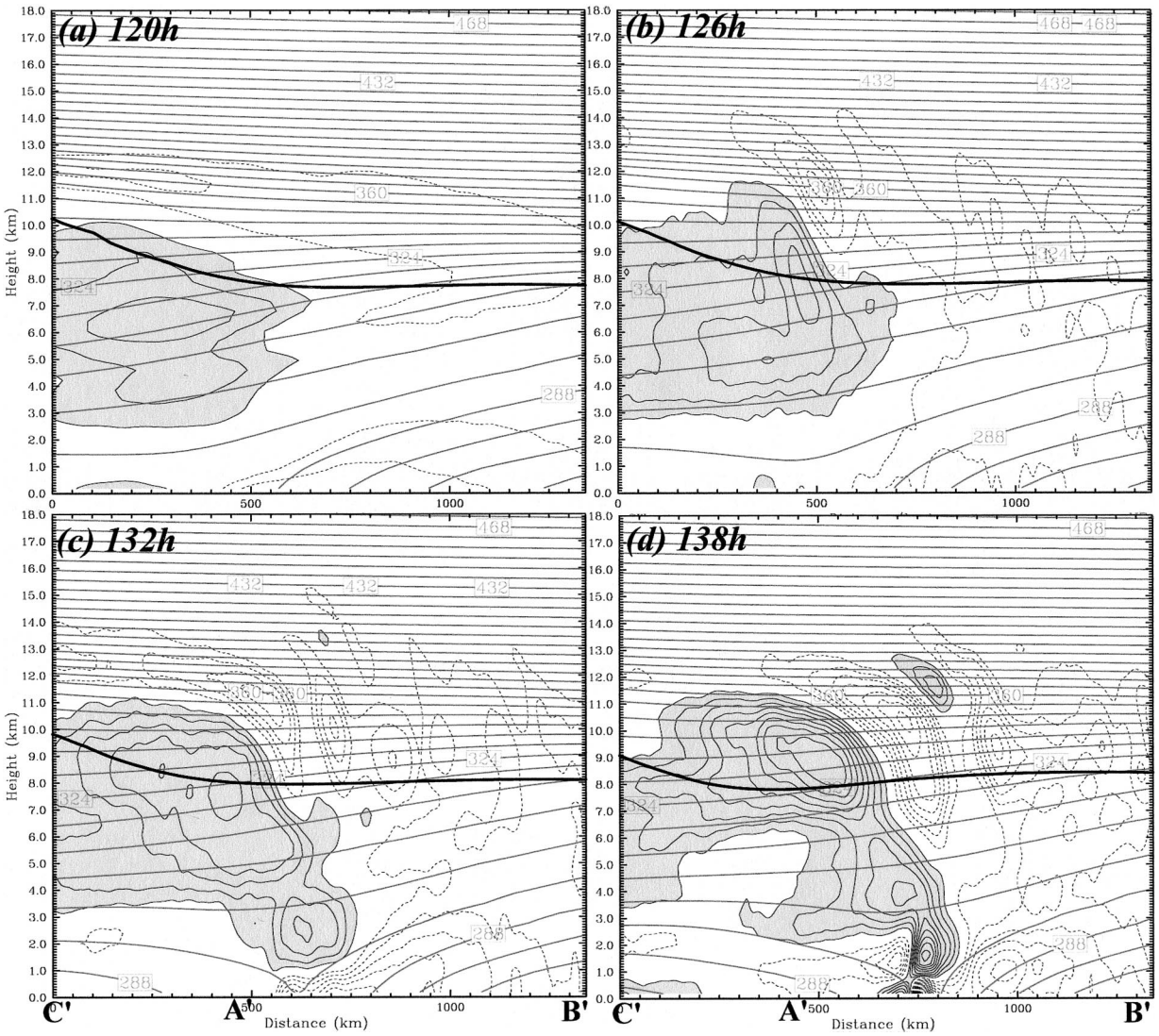

FIG. 12. The residual of the nonlinear balance equation (solid, positive; dashed, negative; $\Delta = 2 \times 10^{-10}$ s^{-2}) and potential temperature (thick line, $\Delta = 5$ K) simulated in DIFFUS, valid at (a) 120, (b) 126, (c) 132, and (d) 138 h along the cross section C′B′ of Fig. 9a. The bold curve denotes the location of dynamic tropopause.

formulated as an initial value problem with geostrophy as the underlying balance, the flow should be restored to balance after radiating away unbalanced energy through gravity waves. In the current study, as demonstrated from Figs. 10–11, the imbalance becomes increasingly strong even after the gravity waves are generated. This seeming controversy can be reconciled if continuous production of imbalance by the background flow (quasi-balanced slow manifold) through quasi-balance evolution (e.g., Raymond 1992) is greater than the reduction of imbalance through balance adjustment. In this case, the flow can become increasingly unbalanced while the gravity waves are being generated. In other words, the continuous production of imbalance by the background flow and the balance adjustment to restore balance through radiation of gravity waves becomes two inseparable counteracting processes. Thus, the sustained gravity waves can be looked at as being directly forced by the imbalances that are ultimately forced by the background baroclinic instability (quasi-balanced slow manifold). An analog of such counteracting processes can be found in explaining sustained convection through convective adjustment: continuous destabilization by the background flow can lead to continuous production of convective instability while convective adjustment is releasing available convective potential energy (imbalance energy) through instantaneous initiation of convection.

Similarities and differences exist between our *balance adjustment* hypothesis and the theory of *spontaneous gravity wave emission* directly forced by balance flows (e.g., Lighthill 1952; Ford 1994; Reeder and Griffiths

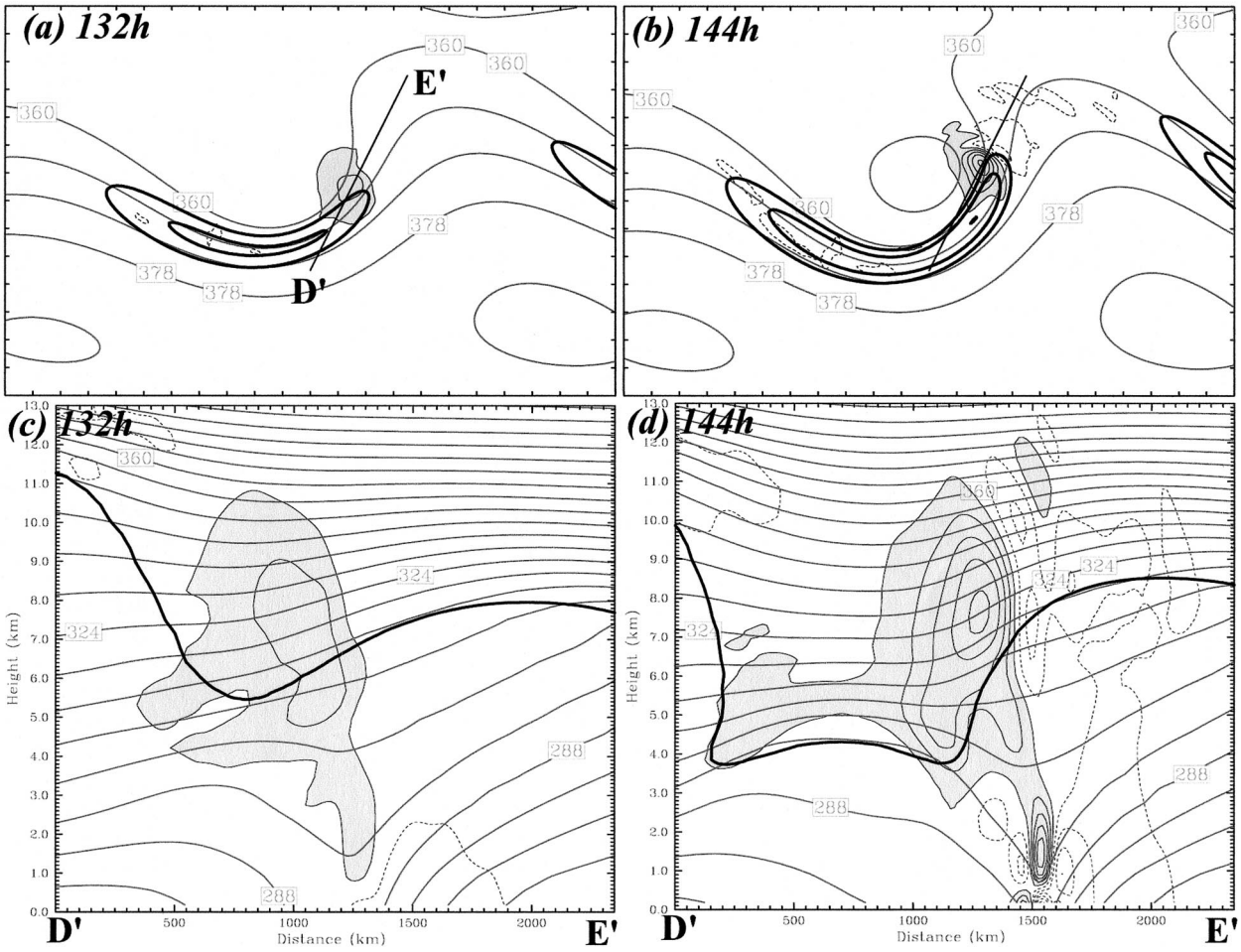

FIG. 13. As in Figs. 10d,e but for (a) 132 and (b) 144 h and Figs. 11d,e but for (c) 132 and (d) 144 h along cross section D′E′ denoted in (a).

1996; McIntyre and Norton 2000; Plougonven and Zeitlin 2002). Both support continuous (spontaneous) wave generation (emission) from the largely balanced (in terms of nonlinear balance) but baroclinically unstable jet–front system. The key difference lies in the existence of imbalance preceding gravity wave generation. Our ΔNBE diagnosis indicates that the initially balanced baroclinic jet–front system will become increasingly unbalanced, leading to subsequent gravity wave generation through adjustment of the imbalance. However, at this point, we cannot rule out the possibility that the imbalance that we diagnose may be explainable with a higher-order balance theory if one exists (Snyder 2003, personal communication). It is also possible that the balanced flows are spontaneously radiating weak gravity waves while producing imbalance in which both processes of wave generation coexist. Other unresolved issues with the balance adjustment hypothesis include 1) how the balanced state and imbalance (including the gravity waves) interact with each other, 2) what the exact dynamical processes are through which the gravity waves are generated by adjustment in terms of the governing equations, and 3) what processes determine the wave characteristics. These issues are currently under investigation.

The upper-tropospheric and stratospheric gravity waves in our simulations also differ from those associated with the upper-level frontogenesis studied by Griffiths and Reeder (1996) in that their wave fronts are initially parallel to the frontal surface (e.g., their Fig. 8) while the current waves are nearly perpendicular to the tropopause (e.g., Fig. 11f). A two-dimensional model was used in their study, which might contribute to the difference. Experiment DIFFUS demonstrated that the simulated upper-tropospheric and stratospheric gravity waves may be generated aloft rather than in direct association with fronts at the surface. However, this is not to say that surface or upper-level frontogenesis is a nonfactor. They are both essential parts of the baroclinic wave life cycle coupling closely with each other; both contribute to the intensification and curvature of the upper-level jet streak and the general flow imbalance crucial for wave generation. Since the primary upper-level gravity waves of interest are also generated right

above a broad region of upward motion associated with the occluding surface fronts, we cannot rule out the possibility that the gravity waves observed aloft may be forced by the strong frontal uplifting partially due to the surface fronts. Indeed, in the high-resolution experiments this seems to be increasingly the case as time progresses.

7. Summary and conclusions

In this study, the PSU–NCAR MM5 model with extremely high resolutions (up to 3.3-km horizontal grid spacing and 180-m vertical grid spacing) is used to simulate the generation of mesoscale gravity waves from the life cycle of baroclinic jet–front systems. The model is initialized with a balanced 2D channeled baroclinic jet and a balanced 3D initial perturbation derived from PV inversion. Long-lived vertically propagating mesoscale gravity waves originating from the exit region of the upper-tropospheric jet streak with horizontal wavelengths ~100–200 km are for the first time unambiguously simulated in a manner consistent with past observational studies (e.g., Thomas et al. 1999) and the conceptual model of UK87. Sensitivity experiments show that the characteristics of these mesoscale waves do not strongly depend on the model resolution, although even smaller-scale variations are produced beyond the predominant mesoscale gravity waves in the higher-resolution simulations.

The residual of the nonlinear balance equation is found to be a useful index in diagnosing flow imbalance and predicting gravity wave generation. From the diagnosis of the flow imbalance, *balance adjustment*, as a generalization of the geostrophic adjustment hypothesis, is proposed to be the likely mechanism in generating these mesoscale gravity waves in the unbalanced upper-tropospheric jet–front systems. In this hypothesis, the flow can become increasingly unbalanced while the gravity waves are being generated if the production of imbalance by the background flow outweighs the reduction of imbalance through the radiation of gravity waves.

Acknowledgments. I am grateful to Chris Davis for providing the codes for PV inversion and to Jim Bresch, Jimy Dudhia, Wei Wang, and Zhe-Min Tan for their help on setting up the idealized simulations. Thanks are also due to discussions with and/or comments from Joan Alexander, Lance Bosart, H.-Y. Chun, Phil Cunningham, Chris Davis, Tim Dunkerton, Craig Epifanio, Dan Keyser, Mike Kaplan, Steve Koch, Todd Lane, Chungu Lu, Dave Muraki, John Nielsen-Gammon, Riwal Plougonven, Jordan Powers, Mohan Ramamurthy, Michael Reeder, Rich Rotunno, Mel Shapiro, and Chris Snyder. Informal reviews by Epifanio, Kaplan, Lane, and Nielsen-Gammon, and formal reviews by Dunkerton, Snyder, and another anonymous reviewer on earlier versions of the manuscript were thorough and helpful. This research was supported by NSF Grant ATM-0203238.

REFERENCES

Allen, J. S., 1991: Balance equations based on momentum equations with global invariants of potential enstrophy and energy. *J. Phys. Oceanogr.,* **21,** 265–276.

Blumen, W., 1972: Geostrophic adjustment. *Rev. Geophys. Space Phys.,* **10,** 485–528.

Bosart, L. F., W. E. Bracken, and A. Seimon, 1998: A study of cyclone mesoscale structure with emphasis on a large-amplitude inertia–gravity wave. *Mon. Wea. Rev.,* **126,** 1497–1527.

Cahn, A., 1945: An investigation of the free oscillations of a simple current system. *J. Meteor.,* **2,** 113–119.

Charney, J. G., 1955: The use of primitive equations of motions in numerical predictions. *Tellus,* **7,** 22–26.

Davis, C. A., and K. A. Emanuel, 1991: Potential vorticity diagnosis of cyclogenesis. *Mon. Wea. Rev.,* **119,** 1929–1952.

Dudhia, J., 1993: A nonhydrostatic version of the Penn State/NCAR mesoscale model: Validation tests and simulation of an Atlantic cyclone and cold front. *Mon. Wea. Rev.,* **121,** 1493–1513.

Dunkerton, T. J., 1997: Shear instability of internal inertia–gravity waves of baroclinic instability. *J. Atmos. Sci.,* **54,** 1628–1641.

Eliassen, A., and E. Palm, 1960: On the transfer of energy in stationary mountain waves. *Geofys. Publ.,* **22,** 1–23.

Ford, R., 1994: The response of a rotating ellipse of uniform potential vorticity to gravity wave radiation. *Phys. Fluids,* **6,** 3694–3704.

Fritts, D. C., 1984: Shear excitation of atmospheric gravity waves. Part II: Nonlinear radiation from a free shear layer. *J. Atmos. Sci.,* **41,** 524–537.

——, and Z. Luo, 1992: Gravity wave excitation by geostrophic adjustment of the jet stream. Part I: Two-dimensional forcing. *J. Atmos. Sci.,* **49,** 681–697.

——, and G. D. Nastrom, 1992: Sources of mesoscale variability of gravity waves. Part II: Frontal, convective, and jet stream excitation. *J. Atmos. Sci.,* **49,** 111–127.

Gent, P., and J. C. McWilliams, 1982: Intermediate model solutions to the Lorenz equations: Strange attractors and other phenomena. *J. Atmos. Sci.,* **39,** 3–13.

Grell, G. A., J. Dudhia, and D. R. Stauffer, 1994: A description of the fifth-generation Penn State/NCAR mesoscale model (MM5). NCAR Tech. Note NCAR/TN-398+STR, 122 pp.

Griffiths, M. A., and M. J. Reeder, 1996: Stratospheric inertia–gravity waves generated in a numerical model of frontogenesis. I: Model solutions. *Quart. J. Roy. Meteor. Soc.,* **122,** 1153–1174.

Holton, J. R., P. H. Haynes, M. E. McIntyre, A. R. Douglass, R. B. Road, and L. Pfister, 1995: Stratosphere–troposphere exchange. *Rev. Geophys.,* **33,** 403–439.

Hooke, W. H., 1986: Gravity waves. *Mesoscale Meteorology and Forecasting,* P. S. Ray, Ed., Amer. Meteor. Soc., 272–288.

Hoskins, B. J., M. E. McIntyre, and A. W. Robertson, 1985: On the use and significance of isentropic potential vorticity maps. *Quart. J. Roy. Meteor. Soc.,* **111,** 877–946.

Kaplan, M. L., and D. A. Paine, 1977: The observed divergence of the horizontal velocity field and pressure gradient force at the mesoscale. *Beitr. Phys. Atmos.,* **50,** 321–330.

——, S. E. Koch, Y.-L. Lin, R. P. Weglarz, and R. A. Rozumalski, 1997: Numerical simulations of a gravity wave event over CCOPE. Part I: The role of geostrophic adjustment in mesoscale jetlet formation. *Mon. Wea. Rev.,* **125,** 1185–1211.

Keyser, D., and M. A. Shapiro, 1986: A review of the structure and dynamics of upper-level frontal zones. *Mon. Wea. Rev.,* **114,** 452–499.

Koch, S. E., and P. B. Dorian, 1988: A mesoscale gravity wave event observed during CCOPE. Part III: Wave environment and probable source mechanisms. *Mon. Wea. Rev.,* **116,** 2570–2592.

——, F. Zhang, M. Kaplan, Y.-L. Lin, R. Weglarz, and M. Trexler, 2001: Numerical simulation of a gravity wave event observed

during CCOPE. Part III: Mountain–plain solenoids in the generation of the second wave episode. *Mon. Wea. Rev.*, **129,** 909–932.
Koppel, L. L., L. F. Bosart, and D. Keyser, 2000: A 25-yr climatology of large-amplitude hourly surface pressure changes over the conterminous United States. *Mon. Wea. Rev.*, **128,** 51–68.
Lane, T. P., and M. J. Reeder, 2001: Convectively generated gravity waves and their impacts on the cloud environment. *J. Atmos. Sci.*, **58,** 2427–2440.
Lighthill, J. M., 1952: On sound generated aerodynamically. Part I. General theory. *Proc. Roy. Soc. London*, **A211,** 564–587.
Lindzen, R. S., 1974: Wave–CISK in the tropics. *J. Atmos. Sci.*, **31,** 156–179.
——, and M. Fox-Rabinovitz, 1989: Consistent vertical and horizontal resolution. *Mon. Wea. Rev.*, **117,** 2575–2583.
McIntyre, M. E., and W. A. Norton, 2000: Potential vorticity inversion on a hemisphere. *J. Atmos. Sci.*, **57,** 1214–1235.
O'Sullivan, D., and T. J. Dunkerton, 1995: Generation of inertia–gravity waves in a simulated life cycle of baroclinic instability. *J. Atmos. Sci.*, **52,** 3695–3716.
Plougonvon, R., and V. Zeitlin, 2002: Internal gravity wave emission from a pancake vortex: An example of wave–vortex interaction in strongly stratified flows. *Phys. Fluids*, **14,** 1259–1268.
Powers, J. G., 1997: Numerical model simulations of a mesoscale gravity wave event: Sensitivity tests and spectral analyses. *Mon. Wea. Rev.*, **125,** 1838–1869.
——, and R. J. Reed, 1993: Numerical model simulation of the large-amplitude mesoscale gravity-wave event of 15 December 1987 in the central United States. *Mon. Wea. Rev.*, **121,** 2285–2308.
Ramamurthy, M. K., R. M. Rauber, B. Collins, and N. K. Malhotra, 1993: A comparative study of large-amplitude gravity-wave events. *Mon. Wea. Rev.*, **121,** 2951–2974.
Rauber, R. M., M. Yang, M. K. Ramamurthy, and B. F. Jewett, 2001: Origin, evolution, and fine-scale structure of the St. Valentine's Day mesoscale gravity wave observed during STORM-FEST. Part I: Origin and evolution. *Mon. Wea. Rev.*, **129,** 198–217.
Raymond, D. J., 1976: Wave–CISK and convective mesosystems. *J. Atmos. Sci.*, **33,** 2392–2398.
——, 1992: Nonlinear balance and potential vorticity thinking at large Rossby number. *Quart. J. Roy. Meteor. Soc.*, **118,** 987–1105.
Reeder, M. J., and M. A. Griffiths, 1996: Stratospheric inertia–gravity waves generated in a numerical model of frontogenesis. I: Model solutions. *Quart. J. Roy. Meteor. Soc.*, **122,** 1175–1195.
Rossby, C. G., 1938: On the mutual adjustment of pressure and velocity distributions in certain simple current systems. *J. Mar. Res.*, **7,** 239–263.
Rotunno, R., and J.-W. Bao, 1996: A case study of cyclogenesis using a model hierarchy. *Mon. Wea. Rev.*, **124,** 1051–1066.
——, W. C. Skamarock, and C. Snyder, 1994: An analysis of frontogenesis in numerical simulations of baroclinic waves. *J. Atmos. Sci.*, **51,** 3373–3398.
Schneider, R. S., 1990: Large-amplitude mesoscale wave disturbances within the intense midwest extratropical cyclone of 15 December 1987. *Wea. Forecasting*, **5,** 533–558.
Shapiro, M. A., 1981: Frontogenesis and geostrophically forced secondary circulations in the vicinity of jet stream–frontal zone systems. *J. Atmos. Sci.*, **38,** 954–973.
——, and D. Keyser, 1990: Fronts, jet streams, and the tropopause. *Extratropical Cyclones: The Erik Palmen Memorial Volume*, C. W. Newton and E. O. Holopainen, Eds., Amer. Meteor. Soc., 167–191.
Snyder, C., W. C. Skamarock, and R. Rotunno, 1993: Frontal dynamics near and following frontal collapse. *J. Atmos. Sci.*, **50,** 3194–3211.
Thomas, L., R. M. Worthington, and A. J. McDonald, 1999: Inertia–gravity waves in the troposphere and lower stratosphere associated with a jet stream exit region. *Ann. Geophys.*, **17,** 115–121.
Uccellini, L. W., and S. E. Koch, 1987: The synoptic setting and possible source mechanisms for mesoscale gravity wave events. *Mon. Wea. Rev.*, **115,** 721–729.
Van Tuyl, A. H., and J. A. Young, 1982: Numerical simulation of nonlinear jet streak adjustment. *Mon. Wea. Rev.*, **110,** 2038–2054.
Wandishin, M. S., J. W. Nielsen-Gammon, and D. Keyser, 2000: A potential vorticity diagnostic approach to upper-level frontogenesis within a developing baroclinic wave. *Mon. Wea. Rev.*, **128,** 3918–3938.
Zhang, F., and S. E. Koch, 2000: Numerical simulation of a gravity wave event observed during CCOPE. Part II: Wave generation by an orographic density current. *Mon. Wea. Rev.*, **128,** 2777–2796.
——, S. E. Koch, C. A. Davis, and M. L. Kaplan, 2000: A survey of unbalanced flow diagnostics and their application. *Adv. Atmos. Sci.*, **17,** 165–183.
——, ——, ——, and ——, 2001: Wavelet analysis and the governing dynamics of a large-amplitude gravity wave event along the east coast of the United States. *Quart. J. Roy. Meteor. Soc.*, **127,** 2209–2245.
——, ——, and M. L. Kaplan, 2003: Numerical simulations of a large-amplitude gravity wave event along the east coast of the United States. *Meteor. Atmos. Phys.*, in press.